Full length article

The dual role of boron on hydrogen embrittlement: example of interface-related hydrogen effects in an austenite-ferrite two-phase lightweight steel

Xizhen Dong [a] , Shaolou Wei [a] , Ali Tehranchi [a] , Aparna Saksena [a] , Dirk Ponge [a] , Binhan Sun [b,c,*] , Dierk Raabe [a,*]

[a] *Max-Planck-Institut für Sustainable Materials GmbH, Max-Planck-Straße 1, Düsseldorf 40237, Germany*
[b] *Key Laboratory of Pressure Systems and Safety, Ministry of Education, School of Mechanical and Power Engineering, East China University of Science and Technology, Shanghai 200237, China*
[c] *State Key Laboratory of Chemical Safety, East China University of Science and Technology, Shanghai 200237, China*

ARTICLE INFO

ABSTRACT

Fe-Mn-Al-C steels are of interest because of their low weight and the wide tunability of their strength-ductility combinations. Despite their high mechanical strength, these advanced steels, particularly when equipped with a multiphase microstructure, are often prone to hydrogen embrittlement (HE), a phenomenon characterized by the abrupt loss of the materials' load-bearing capacity resulting from H ingress. This motivates us to develop strategies to make these alloys HE resistant. Here, we investigate and quantify the influence of interfacial B segregation on the HE resistance in a typical high-Mn, high-Al lightweight steel with a two-phase austenite-ferrite microstructure. Unlike the commonly reported beneficial role of B segregation in suppressing H-induced damage in single-phase alloys, we reveal that B segregation in the studied steel can lead to both detrimental and beneficial effects. On the one hand, it suppresses H-induced cracking along austenite-ferrite phase boundaries, primarily due to segregation-mediated interface strengthening. On the other hand, B segregation appears to promote H diffusion, increasing H contamination across wider microstructure regions and facilitating HE by H-induced cleavage fracture within ferrite—an alternative damage mode to interface cracking. The ingress and penetration of microstructures by H are closely connected with the kinetics and trapping features of H transport along grain boundaries (GBs, γ/γ and α/α) and phase boundaries (α/γ). We observe that interfacial H diffusion can be enhanced in B-doped steels, due to the repulsion and competition between segregated B and H atoms, as exemplified by *ab initio* calculations. The interplay between these two effects, resulting from interfacial B segregation, leads to an overall diminished HE resistance in the studied material compared to its B-free counterpart. These findings underscore the mechanistic complexity of B segregation in influencing HE resistance in multiphase steels, highlighting its dual role that must be accounted for in the development of future H-tolerant alloys.

1. Introduction

There is a growing demand for steels with high strength, improved energy absorption and lower mass density, to reconcile environmental needs with improvement of passenger safety in the automotive sector. Hence, intense efforts are devoted to the development of advanced high-strength steels (AHSSs) [1,2]. One approach lies in incorporating Al (up to 12 wt. %) into Fe-Mn-C steels, enabling low mass density at maintained formability and strain hardening, without compromising safety,

e.g. in terms of the material's energy adsorption capability [3,4]. This alloy design concept matured into the family of Fe-Mn-Al-C lightweight steels. These steels can be classified into three categories based on their microstructures: ferritic [5], austenitic [6–8] and austenite-ferrite duplex [8–10]. Of these, steels with a two-phase microstructure are tunable for a broad spectrum of strength-ductility combinations. They typically contain a high Mn content (18–30 wt. %) to stabilize the austenite phase to ambient temperatures and below [8,9]. This also reduces the stacking fault energy and thus gives access to high strain

---

hardenability due to the activation of transformation-induced plasticity, twinning-induced plasticity and/or extensive dislocation planar slip within the austenite, enabling an excellent strength-ductility product [2–4,6–11]. However, with increasing strength levels in AHSSs, a severe issue of hydrogen embrittlement (HE) arises. This is defined as the abrupt degradation of a material's load-bearing capacity when exposed to H [9,12–14], which raises strong concerns for the application of these steels.

In contrast to single-phase materials, effective strategies for mitigating HE in lightweight multiphase steels remain scarce [9,12,13]. This is primarily due to the multiple phases and hetero-interfaces present in these steels, leading to complex and often competing H transport phenomena, H trapping and H-induced damage modes as well as embrittling mechanisms associated with the different phases and interface types, features that are difficult to predict, balance and control. Despite these, fundamental understanding of H-induced damage mechanisms in these materials remains limited, with only a few studies available to date [12]. In this regard, our preceding study of a high-Mn, high-Al austenite-ferrite lightweight steel underpinned H-induced intergranular cracking at austenite-ferrite phase boundaries and cleavage cracking within the ferrite phase, which jointly act as the governing embrittlement mechanisms [9]. The intergranular fracture was attributed to the H-enhanced decohesion mechanism at phase boundaries. The latter damage effect was associated with decohesion and plasticity-mediated embrittlement within ferrite phase.

Commonly documented HE mitigating strategies in high-strength steels include second-phase/precipitate trapping [15,16], grain refinement [17–19], grain boundary (GB) engineering [20–22] and solute segregation/heterogeneity engineering [14,23–25]. Among these approaches, solute segregation engineering has been developed to optimize the intrinsic properties of interfaces, aiming to suppress H-induced interface failure. Notably, B stands out due to its vital role in enhancing GB cohesive strength, exerting a profound influence on HE resistance improvement in various materials, including Ni-based alloys, martensitic steels and medium-entropy alloys [26–28]. In addition to the enhancing effect on interface cohesive strength, B segregation at interfaces was also reported to facilitate slip transfer, which effectively relieves the forward stress imposed by dislocation pile-ups at grain boundaries [26,27]. These factors, associated with B segregation, have been shown to be effective in mitigating HE, as validated by numerous studies [26–29]. However, these studies have primarily focused on single-phase materials, where failure is mostly driven by H-induced intergranular decohesion along GBs. In multiphase steels with more complex H-induced damage modes, on the other hand, the effectiveness of interface B segregation remains ambiguous. It is hence highly motivated to establish a better understanding of the influence of B segregation on the HE behavior in these materials.

In this study, we focus on a B-doped high Mn lightweight steel with an austenite-ferrite two-phase microstructure. Contrary to the previously reported advantageous effect of B segregation at austenite GBs, this study reveals an unexpected and counterintuitive outcome, where B doping plays a detrimental role on the alloys' overall HE resistance, despite the suppressed H-induced interface cracking. This unforeseen result challenges our established understanding and highlights the complexity of the interactions between B, H and the multiple interfaces, including grain- and phase boundaries (γ/γ, α/α and α/γ) of multiphase alloys, particularly in terms of the role of segregated B on H trapping and H transport.

To address these phenomena and their interplay, we first examined the segregation behavior of B at both ferrite and austenite GBs and at phase boundaries through correlative transmission Kikuchi diffraction (TKD) electron microscopy and atom probe tomography (APT) analyses [9,30,31]. A combination of damage characterization and *ab initio* calculations of B and H segregation energy at a ferrite GB was used to investigate the effect of B segregation on the HE behavior. A fundamental microstructure-informed design concept for H-tolerant alloys

was also discussed in the final part of the paper.

2. Experiments

2.1. Material and processing

A B-doped high-Mn and high-Al lightweight steel with a nominal chemical composition of Fe-19.8Mn-9Al-0.64C-0.009B wt. %, was fabricated. The melt was prepared in a vacuum induction furnace and cast into a 4 kg ingot. Following homogenization at 1100°C for 2 h, the ingot was hot-rolled to a thickness of approximately 3.2 mm at 1100°C, followed by air cooling to room temperature. The hot-rolled sheets were next cold rolled to a final thickness of ~1.6 mm. Specimens prepared from cold-rolled sheets were annealed at 1100°C for 10 min under Ar atmosphere and quenched in water to room temperature. A B-free reference steel for comparison was prepared applying the same protocol.

2.2. Hydrogen charging and mechanical testing

Electrochemical H pre-charging was carried out using the three-electrode method, where an aqueous solution containing 3 wt. % NaCl and 0.3 wt. % NH$_4$SCN was selected as the electrolyte. A platinum foil was employed as the counter electrode and a KCl-saturated Ag/AgCl electrode served as the reference electrode. The applied current density was 5 A/m^2. The charging time ranged from 0 to 72 h to estimate the effective H diffusivity. Samples for mechanical testing were charged for 24 h. Note that all pre-charged samples were ground prior to charging to guarantee a clean and fresh surface. Tensile specimens were fabricated with a gauge length of 4 mm, a gauge width of 2 mm, and a thickness of 1.2 mm. Slow strain rate tensile tests (10^{-4} s^{-1}) were performed on the pre-charged and non-charged specimens using a Kammrath & Weiss stage (GmbH, Dortmund, Germany). Digital image correlation (DIC) was employed to measure both global and local strain and all tensile tests were carried out at least 3 times.

A thermal desorption spectrometer (TDS, G8 GALILEO MS) equipped with an infrared furnace and a mass spectrometer was used to quantify diffusible H content and investigate the nature of H trapping and desorption. Disk-shaped specimens with a diameter of 10 mm and a thickness of approximately 1.2 mm were prepared, followed by mechanical grinding to remove the oxide layers. The time interval between the completion of H pre-charging and the TDS analysis was kept within 15 min. Gas calibration using a standardized Ar-5 % H$_2$ forming gas was conducted before H measurement to ensure accurate quantification. The desorbed H was collected using the mass spectrometer. The heating rate was set to 16°C/min from room temperature to 800°C, followed by an isothermal hold for 100 s.

2.3. Microstructure characterization

A ZEISS Sigma scanning electron microscope equipped with an electron backscatter diffraction (EBSD) detector was employed to characterize the microstructure, fracture surface and damage features. For all microstructure characterization techniques, samples were prepared following a standard metallographic procedure: grinding, diamond polishing (3 μm and 1 μm) and final polishing using a 50 nm colloidal silica suspension (OPS). EBSD was performed to characterize the crystallographic orientation, phase constitution. The TSL OIM software was used for data acquisition and analysis.

Synchrotron X-ray diffraction (SXRD) was used to qualitatively assess the quantity of the soluble B in both, the B-free and B-doped steels. The experiment was carried out at beamline P02.1 of PETRA III at Deutsches Elektronen-Synchrotron (DESY) in Hamburg, Germany, using a beam energy of 60 keV and wavelength of 0.2074 Å (beam size: 1 mm × 1 mm). The two-dimensional Debby-Scherrer patterns were consequently integrated at 10° azimuthal sectors (85-95°) using a GSAS-II software [32].

Three-dimensional atom probe tomography (APT) was utilized to study the elemental distribution and segregation behavior at various interface regions. The APT specimens were site-specifically prepared using a dual-beam scanning electron microscopy/focused ion beam (SEM/FIB) instrument (FEI Helios Nano-Lab 600/600i) with a Ga source. APT specimens were performed using the standard lift-out procedure [31]. TKD was performed to identify the interface location within the specimen and ensure that the interface was near the specimen apex. The measurement was conducted on LEAP 5000 XR (CAMECA Instruments Inc.). Data were collected in a high-voltage laser pulsing mode with a laser energy of 45 pJ and a pulse rate of 200 kHz. The measurement temperature was kept at 60 K and the detection rate was set to 1 %. The collected APT data were analyzed using the AP Suite 6.1 software.

3. Results

3.1. Microstructure and hydrogen trapping behavior

Fig. 1 (a) displays the pseudo-binary phase diagram for the Fe-0.65C-19.8Mn-xAl-0.009B (in wt. %) steel system. The temperature and composition range of the austenite-ferrite two-phase domain well aligns with the B-free reference alloy reported elsewhere [9]. The volume fraction of the respective phases as a function of temperature is displayed in Fig. 1 (b) for both, the B-doped and B-free samples. The high degree of similarity indicates that B addition does not perturb the global phase equilibrium as no boride is observed. Note that these calculation results based on bulk thermodynamics discard the presence of interfaces

and hence cannot be utilized to infer local solute segregation tendency. The as-annealed B-doped sample shows an austenite-ferrite two-phase microstructure, as revealed by the EBSD phase and inverse pole figure (IPF) maps in Fig. 1 (c). The volume fraction of the ferrite is determined to be 28 vol. %, closely matching that of the B-free sample, 26 vol. %. Compared to the average grain size of the ferrite ($\sim$5.2 μm) in the B-free sample [9], the ferrite in the B-doped material exhibits a similar average grain size of $\sim$6.6 μm. The austenite in both steels has a larger grain size than ferrite, with $\sim$11.5 μm for the B-free sample and $\sim$12.3 μm for the B-doped sample (Fig. 1 (c)). SXRD analyses show that the FCC lattice constants of both B-free (3.667 Å) and B-doped (3.665 Å) materials remain comparable. Similarly, B doping does not change the lattice parameters of the BCC phase, 2.905 Å and 2.903 Å for the B-free and B-doped samples, respectively (Fig. S1). These observations, according to Vegard's linear mixture rule, imply a negligible difference in the amount of soluble B within the B-free and B-doped dilute solution with limited B solubility, well aligning with the APT analysis presented next. Because of the high intrinsic stacking fault energy ($>$70 mJ/m^2, Fig. S2, computational details follow [33]), the austenite phase is mechanically stable, and no signs of mechanically-induced twinning or martensitic transformation were observed within the resolution limits of SXRD and EBSD [9,11,31].

3.2. B segregation at ferrite GBs, austenite GBs and hetero-interfaces

The spatially resolved local composition of B in both, the B-free reference steel and in the B-doped steel was examined by APT. The phase information and crystallographic feature of a representative B-free APT
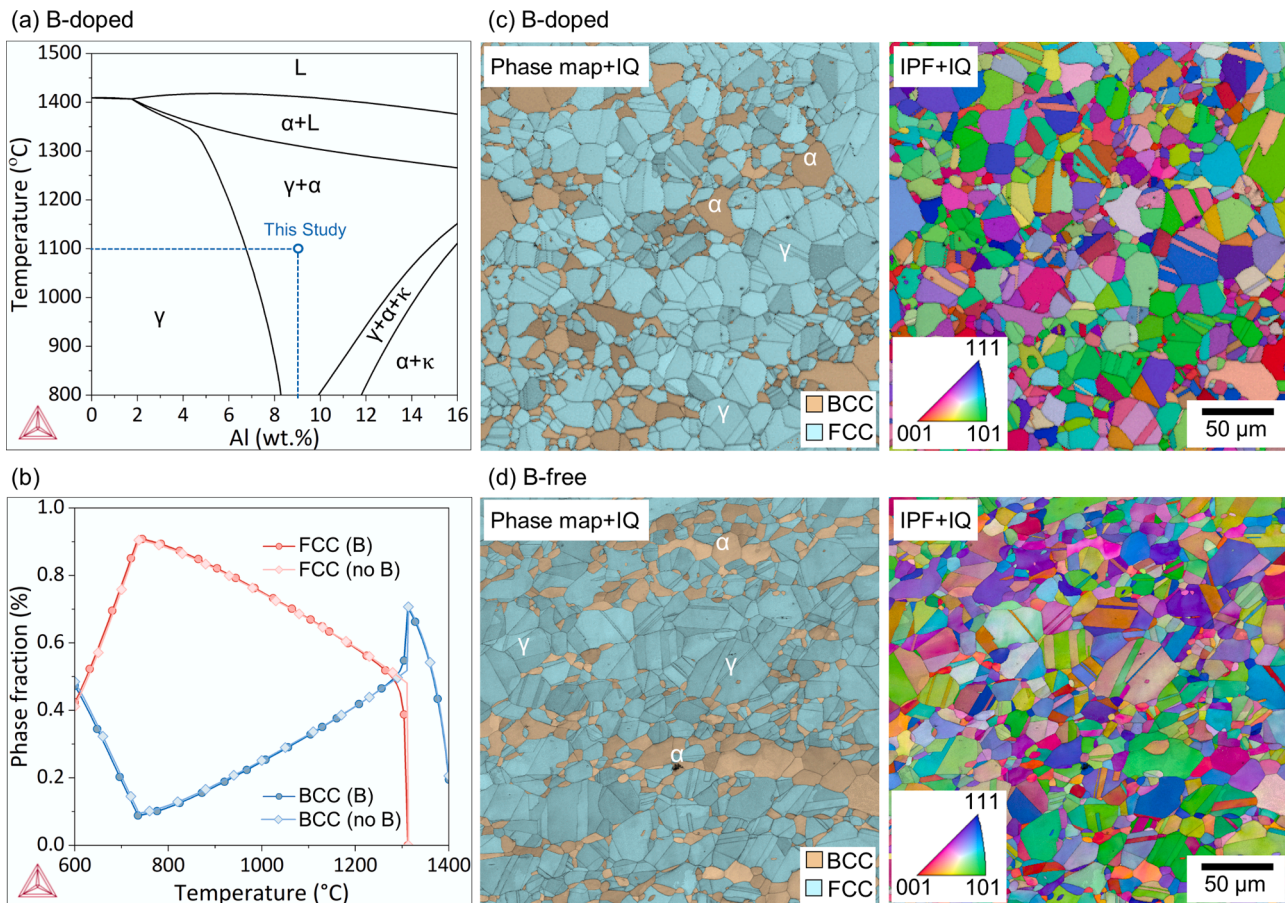

Fig. 1. (a) Pseudo-binary equilibrium phase diagram for the investigated B-doped steel, Fe-0.65C-19.8Mn-xAl-0.009B (wt. %); (b) The equilibrium phase fractions as a function of temperature in the B-doped and B-free materials. Calculations were conducted using Thermo-Calc software with the TCFE11 database; (c) Electron backscatter diffraction (EBSD) imaging (phase plus image quality (IQ) maps and inverse pole figure (IPF) plus IQ maps) of the heat-treated lightweight steel with B (c) and without B (d).

specimen containing a phase boundary, probed by preceding TKD analysis, are shown in Fig. 2 (a). The corresponding 3D-atomic mapping in Fig. 2 (b) shows the atomic distributions of Fe, Al, Mn, and C, revealing their partitioning between ferrite and austenite, as quantitatively depicted in the 1D concentration profiles in Fig. 2 (c). The atomic map of B is also given in Fig. 2 (b), yet, it has to be noted that B in this sample comes from metallurgical impurity (*i.e.,* it was not intentionally added). A minor enrichment of B (~0.06 at. %) at the phase boundary is observed (Fig. 2 (c)), whereas the average B concentration is ~0.014 ±0.006 at. % and ~0.010±0.005 at. % in the probed austenite and ferrite from different regions, respectively, as shown in Table 1.

Similarly, the TKD analyses in Fig. 3 (a), including an IPF and phase map, confirm the presence of a α/γ phase boundary of the B-doped sample. The APT analyses of this hetero-interface in Figs. 3 (b) and (c) exhibit the solute partitioning between austenite and ferrite. The chemical composition within the respective phases remains virtually unchanged between samples with and without B doping. The B concentration within both, ferrite (~0.016±0.007 at. %) and austenite (~0.015±0.007 at. %) is low, comparable to that observed in the corresponding phases in the B-free specimen (see Table 1). However, the B-doped specimen shows a pronounced B segregation at the α/γ phase boundary, with a peak concentration of ~1 at. %, significantly higher than that of the B-free reference sample (~0.06 at. %). These comparisons reveal that the addition of B in the studied steel primarily leads to its segregation at phase boundaries without affecting the bulk B concentration.

With respect to B segregation at GBs, corresponding APT results of a representative austenite GB and a ferrite GB with a misorientation angle of 36° and 20°, respectively, are shown in Fig. 4. We observe that B enriches at the austenite GB, reaching a peak concentration of ~0.5 at. %. Segregation at the ferrite boundary is similar (~0.54 at. %). No segregation can be detected at both austenite or ferrite GBs in the B-free

Table 1
Chemical compositions of B in austenite and ferrite of B-free and B-doped (0.009 wt. %) steels.

|		B-free samples	B-doped samples
B (at. %)	Austenite	0.010±0.005	0.015±0.007
	Ferrite	0.014±0.006	0.016±0.007

reference steel (data not shown here for conciseness). Note that no borides were detected in any of the measured APT specimens that were prepared from different regions.

3.3. Hydrogen uptake and tensile results

Fig. 5 (a) displays the H desorption spectra for the B-free and B-doped steels after electrochemical H pre-charging. For the same charging condition (24 h), the B-doped sample exhibits a notably higher amount of H (6.8±2.2 wt ppm) than the B-free sample with a very similar microstructure (4.7±1.8 wt ppm). On the other hand, the desorption profiles in terms of both shape and peak temperatures are nearly identical for both samples. Although the interpretation of TDS peaks and their associated trapping sites is generally quite challenging for multiphase materials [34,35], we can eliminate from these data the possibility of additional trapping sites being introduced by B doping.

Fig. 5 (b) depicts the relationship between H content and charging time. To precisely describe the diffusion process, the diffusion coefficient of H can be estimated using the in-plane boundary condition variant of Fick's diffusion model, under the assumption that surface concentration remains constant and the H diffusion coefficient is H concentration (C_H)-independent [36,37]:
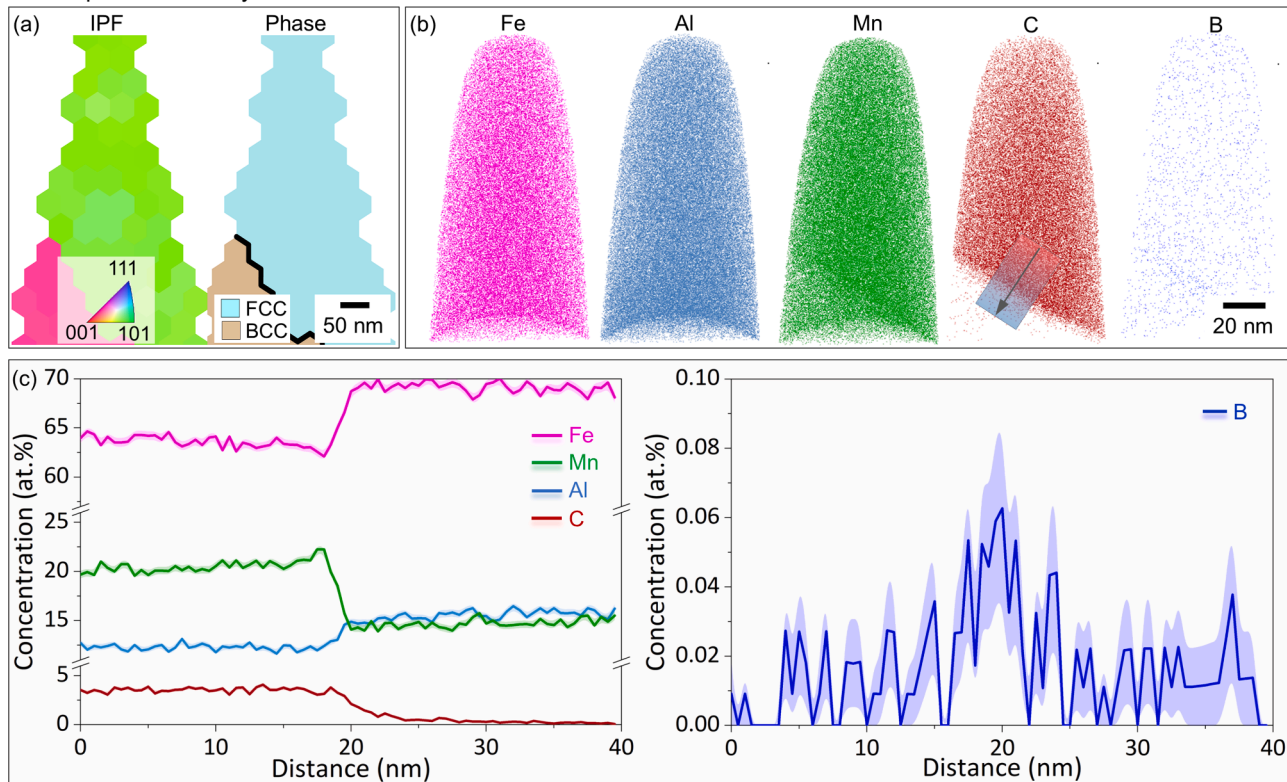
Fig. 2. (a) Transmission Kikuchi diffraction analyses including phase map and inverse pole figure (IPF) and (b) corresponding atom probe tomography analyses containing a α/γ phase boundary in the B-free sample; (c) One-dimensional concentration profiles of Fe, Mn, Al, C and B across the phase boundary along the cylindrical unit (diameter φ: 25 nm) marked in (b).

B-doped: phase boundary
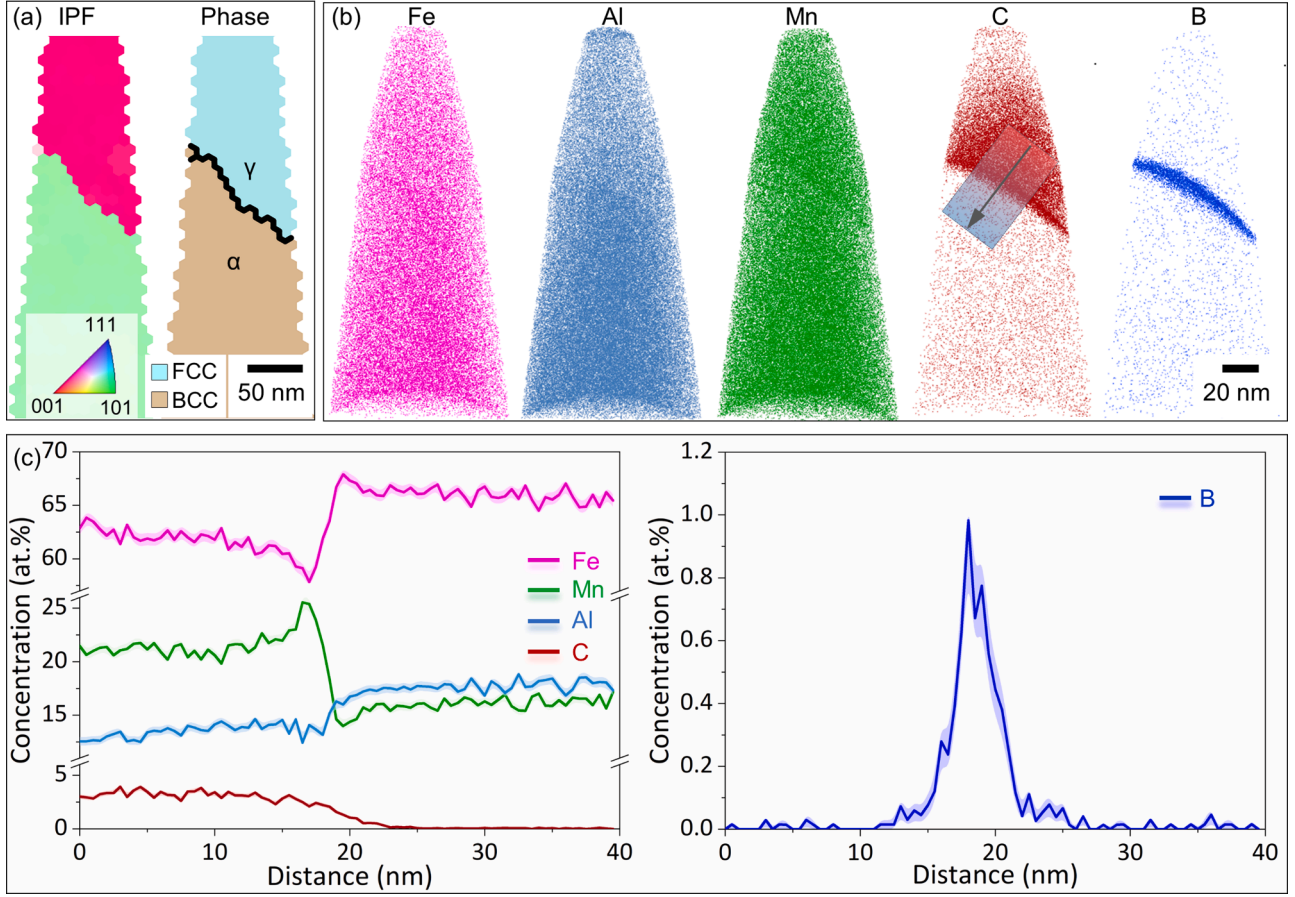
Fig. 3. (a) TKD imaging including phase map and IPF; (b) APT atomic mapping of a typical region containing a α/γ phase boundary in the B-doped sample; (c) One-dimensional concentration profiles of Fe, Mn, Al, C and B across the phase boundary along the cylindrical region with a diameter of 25 nm, indicated in (b).

$$C_{\mathrm{H}} = C_0^{\mathrm{H}} - \frac{4C_0^{\mathrm{H}}}{\pi} \sum_{n=0}^{\infty} \frac{(-1)^n}{2n+1} \exp\left(-\frac{D_{\mathrm{H}}(2n+1)^2 \pi^2 t}{4l^2}\right) \cos\frac{(2n+1)\pi x}{2l} \quad (1)$$

with the boundary conditions defined as:

$$C_{\mathrm{H}}(x=l, \ t \geq 0) = C_0^{\mathrm{H}} \quad (2)$$

$$\frac{\partial C_{\mathrm{H}}}{\partial x}(x=0, \ t \geq 0) = 0 \quad (3)$$

where C_0^{H} represents the constant H concentration at the surface and $2l$ denotes the thickness of the sample. D_{H} refers to the H diffusion coefficient and t is the diffusion time. The total amount of H can be determined by integrating the concentration curve with distance, giving a H content C_{H} as a function of time t:

diffusion coefficient D_{H} and the saturation level C_0^{H} are unknown. The experimentally obtained total amount of H, C_{H}, as presented in Fig. 5 (b), is utilized to determine these parameters using Eq. (4). Unlike in BCC structures, achieving H saturation in FCC-based alloys is particularly challenging due to the 4–6 orders of magnitude lower diffusivity of H in the latter compared to the former phase [38,39], making it challenging to experimentally determine the saturation level. To address this issue, two pending parameters $D_{\mathrm{H}}^{\mathrm{B/no \ B}}$ (the H diffusion coefficient with and without B doping) and C_0^{H}, are estimated by fitting the experimental H content as a function of time. For the B-doped steel, the optimal fit yields $D_{\mathrm{H}}^{\mathrm{B-doped}} \sim 8.3 \times 10^{-16} \ \mathrm{m^2/s}$ and $C_0^{\mathrm{H}} \sim 480$ wtppm. In contrast, the diffusion coefficient is determined as $D_{\mathrm{H}}^{\mathrm{B-free}} \sim 3.0 \times 10^{-16} \ \mathrm{m^2/s}$ under the assumption that the H saturation level is assumed to remain unaltered in the B-free steel. It should be noted that this assumption is reasonable given that the H uptake is primarily attributed to the dis-

$$C_{\mathrm{H}}(t) = C_0^{\mathrm{H}}\left(1 - \frac{4}{\pi^2} \sum_{n=0}^{\infty} \frac{(-1)^n}{2n+1} \exp\left(-\frac{(2n+1)^2 \pi^2 D_{\mathrm{H}} t}{4l^2}\right)\left\{\sin\frac{(2n+1)\pi}{2l} - \sin\left(-\frac{(2n+1)\pi}{2l}\right)\right\}\right) \quad (4)$$

During electrochemical charging, C_0^{H} is generally assumed to be equal to the H saturation level given the continuous and sufficient H supply [36]. In this analytical solution, two key parameters, the

solved H within the austenitic matrix that is not influenced by B-doping [40]. Nevertheless, this calculation suggests a much faster H diffusivity within the B-doped two-phase steel compared with the B-free reference case, which will be further explained in Section 4.2.
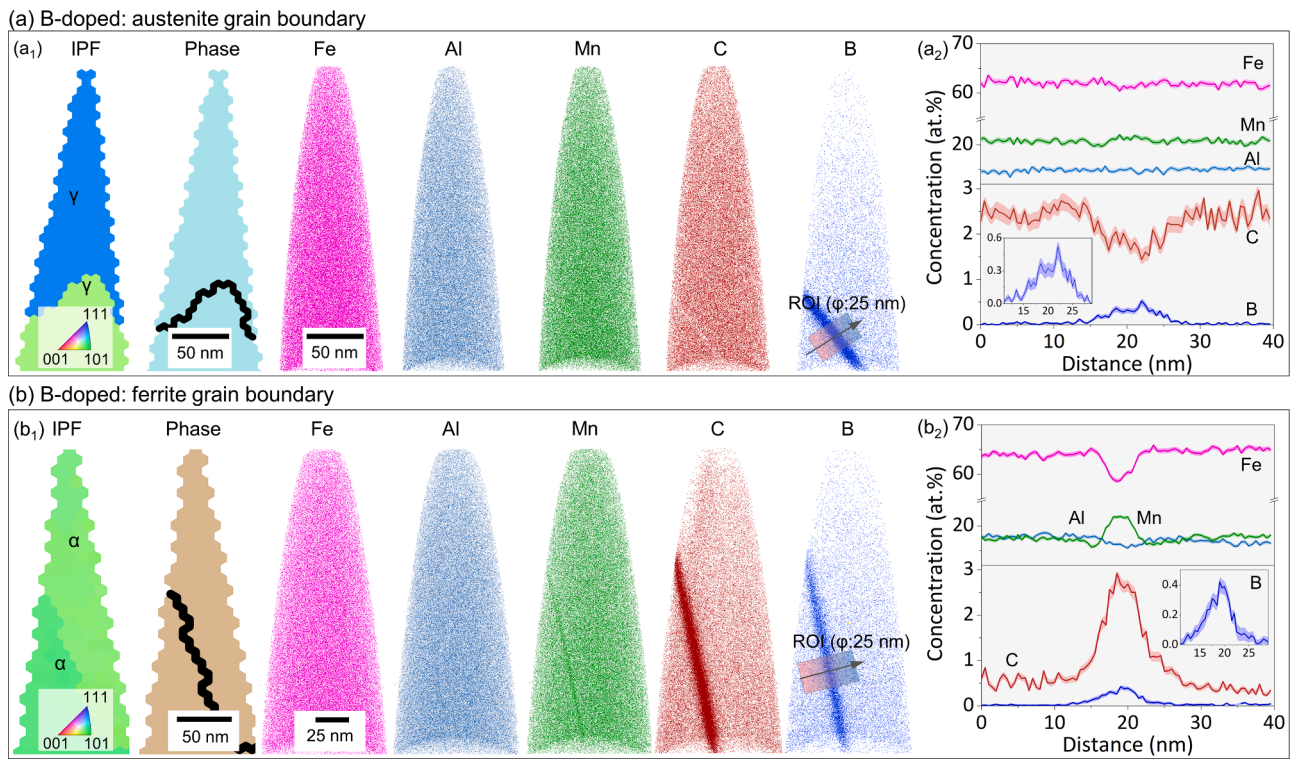
Fig. 4. Correlative TKD (phase and IPF maps) and APT analyses (reconstructed atomic mapping and one-dimension (1D) concentration profile) crossing (a) an austenite grain boundary and (b) a ferrite grain boundary of the investigated B-doped steel. The 1D concentration profile in (a₂) and (b₂) is obtained from the cylindrical unit highlighted in (a₁) and (b₁), respectively. (diameter φ: 25 nm).
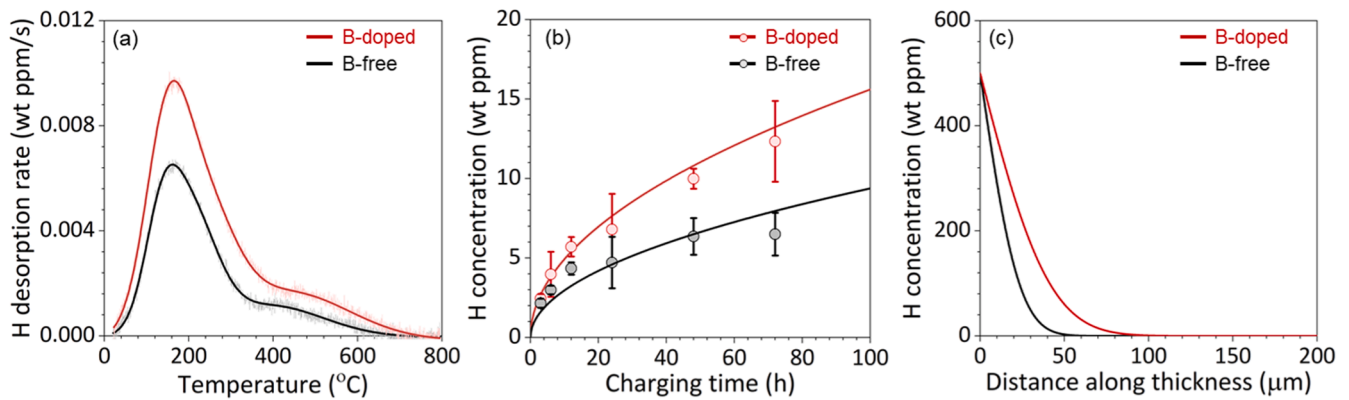

Fig. 5. (a) The representative thermal desorption spectrum (TDS) profiles of H pre-charged samples with and without B doping. The heating temperature ranges from room temperature up to 800°C at a heating rate of 16°C/min; (b) H concentration determined by TDS against charging time with fitting based on an analytical solution of the Fick's law; (c) Calculated H concentration profile along specimen's thickness dimension for the investigated steels subjected to H-charging for 24 h at room temperature. All measurements were conducted at least two times to ensure repeatability.

Furthermore, the inherently sluggish diffusion of H in austenitic steels results in the formation of a steep concentration gradient profile along the sample thickness direction. As shown in Fig. 5 (c), this gradient is predicted based on Eq. (1), incorporating the saturation level and the diffusion coefficients. The concentration profiles elucidate that H diffusion remains insufficient to reach saturation after 24 h of charging for both samples. However, due to the faster H diffusivity in the B-doped sample, H is able to reach deeper region in this sample (~120 μm after 24 h charging) compared with the B-free reference material (~70 μm).

The uniaxial slow-strain rate tensile properties of B-doped and B-free samples, both with and without H pre-charging, are shown in Fig. 6 (a). The yield strength, tensile strength and total elongation are clearly not affected by B doping and associated interface segregation under the non-

charged condition. The detailed mechanical properties are summarized in Table 2. Furthermore, the maximum local strain prior to fracture, measured from the DIC, is also nearly the same between B-free and B-doped samples in the absence of H, as shown in Fig. 6 (b). These findings suggest that the addition of B imposes negligible impact on the tensile properties without H pre-charging.

Fig. 6 (a) shows that the introduction of H does not affect the yield strength for both B-free and B-doped samples. On the contrary, H pre-charging reduces the apparent strain hardening, leading to a degradation in the tensile strength by ~100 MPa for the B-doped sample and ~30 MPa for the B-free sample (Fig. S3). This notable tensile strength reduction is mainly attributed to the H-induced cracks on the specimens' surfaces [9,41]. Compared to the B-free sample, these H-induced surface
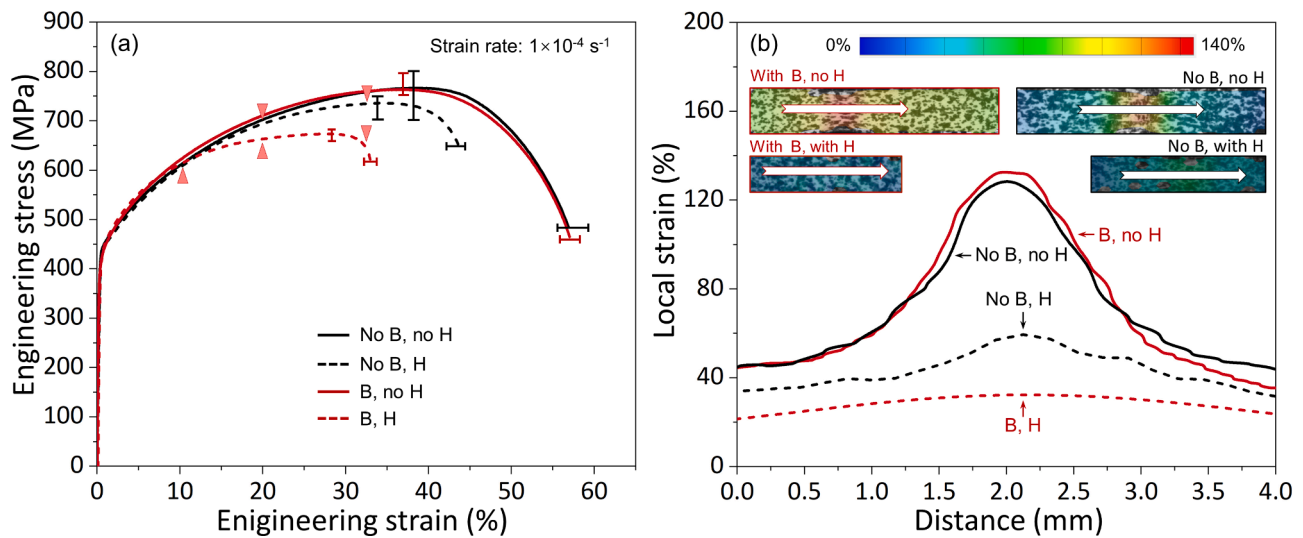
Fig. 6. (a) Mechanical response under uniaxial tensile loading of the B-free and B-doped high-Mn lightweight steels with and without H (strain rate: $1 \times 10^{-4}\,\mathrm{s}^{-1}$). The surface crack evolution as a function of strain, captured using the DIC camera at a frame rate of 0.1 Hz, is depicted in Fig. S4 (indicated by the red triangles); (b) Local tensile strain profiles for the B-doped and B-free reference samples at the point just prior to fracture (the inset showcasing corresponding strain maps and arrows indicating the regions where the profiles were taken). (DIC: digital image correlation) (Engineering stress-strain curves and local strain distribution of B-free reference samples with and without H are reproduced from Ref. [9]).

Table 2
Mechanical properties of the B-free and B-doped materials (0.009 wt. % B) with and without H pre-charging, subjected to uniaxial slow strain rate tensile testing ($1 \times 10^{-4}\,\mathrm{s}^{-1}$, all values are obtained from at least three repeating experiments).

Sample		Yield strength (MPa)	Tensile strength (MPa)	Total elongation (%)	Maximum local strain prior to fracture (%)	Ductility loss due to H (%)
B-free	No H	450±25	752± 53	58.7±2.2	129.7±6.3	–
	With H	440±16	727± 26	42.2±1.6	61.5±4.1	28
B-doping	No H	459±17	782± 22	58.2±1.7	132.4±5.2	–
(0.009 wt. % B)	With H	448±13	675± 12	32.5±0.8	32.6±4.0	44

cracks are developed at an earlier stage (see Fig. S4) for the B-doped sample, at a critical engineering strain of approximately 10 %, whereas they are barely observed at a similar strain level in the B-free sample. This early crack initiation also contributes to the profound drop in elongation, reducing it to 32.5 %, whereas the H-charged B-free reference steel exhibits an average total elongation of 42.2 %. This corresponds to a H-induced ductility loss of ~44 % for the B-doped sample and ~28 % for the B-free reference sample. Pertaining to the local strain, the maximum local strain prior to fracture in the H-charged B-doped sample drops to ~32 % in contrast to ~60 % in the B-free case. These comparisons reveal a higher susceptibility to HE in the B-doped sample. This observation is in sharp contrast to previous studies in single-phase materials, which generally reported a benefical effect of B segregation on HE resistance [26,42–44].

3.4. Hydrogen-induced damage behavior
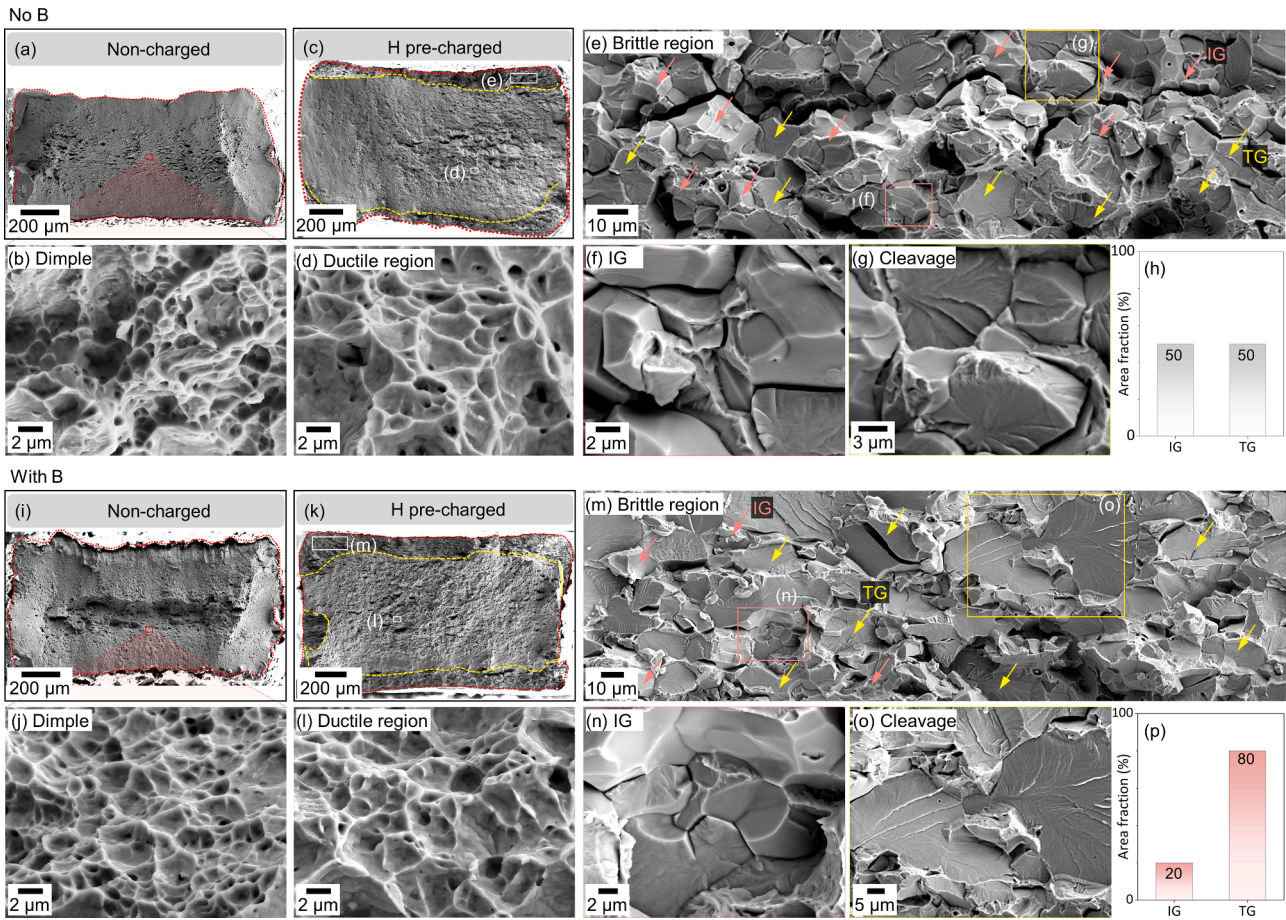
3.4.1. Fractography

To investigate the effect of B segregation on the HE behavior of the steel variants, we studied the fracture and damage mechanisms in both samples in more detail. Under H-free condition, both the B-free and B-doped samples display a predominantly ductile fracture across the entire fracture surface, characterized by the presence of dimples, as shown in Figs. 7 (a) and (i). In contrast, under the presence of H, the fracture surface of both steel types shows two distinct zones: a H-affected brittle zone in the near-surface region (from where the H entered the steel) and a ductile zone in the middle zone (far away from the entrance region of H), as displayed in Figs. 7 (c)-(d) and (k)-(l). It is noteworthy that the depth of the H-induced brittle region in the B-doped sample (~200 μm)

is approximately twice as large as that in the B-free reference material (~120 μm). This finding is consistent with the higher diffusivity of H as well as the higher HE susceptibility found in the B-doped sample. Under the same charging conditions, a higher diffusion coefficient is deemed to result in a greater diffusion distance of at least ~1.6 times, consistent with the larger H-affected brittle region.

The detailed fractography within the H-affected region of the two samples is shown in Figs. 7 (d)-(g) and (l)-(o). For both samples, H-induced intergranular fracture and transgranular cleavage fracture are observed. However, the relative proportion of these two fracture modes is different between the two samples. In the B-free reference steel, intergranular and transgranular cleavage fractures contribute equally to the final embrittlement, each accounting for ~50 % of the brittle region (Fig. 7 (h)). In contrast, for the B-doped sample, intergranular fracture constitutes only ~20 % of the H-affected region, while cleavage fracture dominates, comprising approximately 80 % due to the tortuous crack path propagating preferentially through H-susceptible ferrite, while deflecting from the more resistant austenite and interfaces (Fig. 7 (p)). More specifically, this difference correlates with the interfacial B segregation at ferrite GBs, austenite GBs and ferrite-austenite phase boundaries and its influence on H-induced interface cracking along the above interfaces, which will be discussed in Section 4.1.

3.4.2. H-induced cracking behavior

To further elucidate the H-related fracture behavior, nucleation sites and propagation pathway of H-induced cracking were investigated across the entire gauge section near the surface of H-charged and fractured tensile specimens, with a total of 253 microcracks characterized. For both samples, phase boundaries and ferrite act as critical sites for the formation

Fig. 7. Fractography overview and detailed dimple-type fracture of H-free steels (a)-(b) without B and (i)-(j) with B, respectively. (c) and (k) Fractography overview of the H pre-charged steels. (d)-(e) Magnified images taken from the rectangular frames marked in (c), showing the fracture details in different representative regions in the B-free sample; (f) intergranular fracture; (g) transgranular cleavage fracture. (l)-(o) Magnified images taken from the rectangular frames in (k) and (m) of the B-doped sample. Area fractions of different H-assisted fracture modes (h) without B and (p) with B. (IG: intergranular along grain boundaries and phase boundaries, TG: transgranular cleavage with ferrite phase).
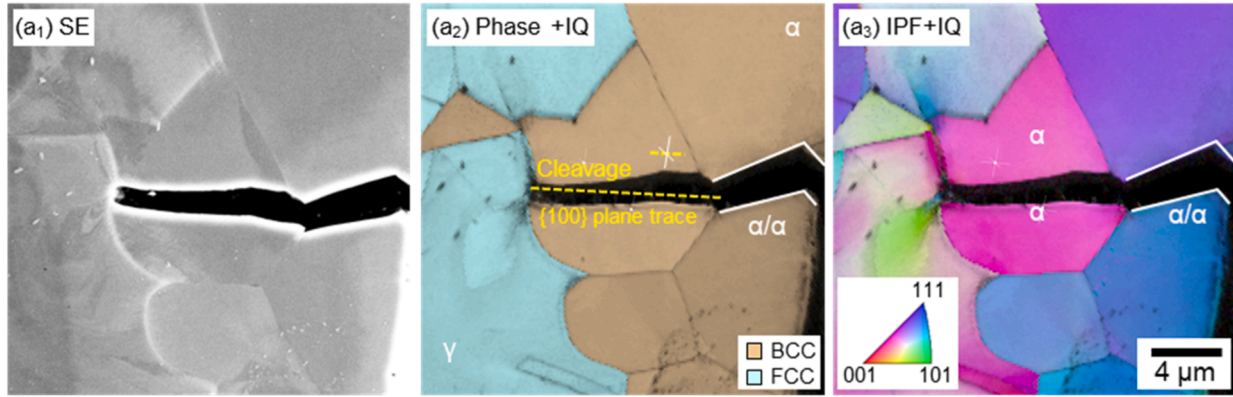
of H-induced cracking. Representative results of the B-doped sample are shown in Fig. 8; the results in the B-free samples are similar and thus not shown here for conciseness (see Fig. S5). The cracks within the ferrite phase are generally observed along the {100} cleavage planes as H accumulation reduces their cohesive strength below the critical stress required for dislocation nucleation, promoting {100} cleavage decohesion [9], as presented in Fig. 8. This observation matches the well-known H-induced transgranular cleavage fracture mode, characterized by the river patterns, resulting from the progressive decohesion of neighboring {100} planes, on the fracture facets, Figs. 7 (g) and (o) [14,45]. To quantify the susceptibility of various cracking incidents, we next reveal statistical comparisons of the crack categories observed in both samples (Fig. 9). Different from the B-free sample where H-induced ferrite cleavage cracking accounts for 40 % of the overall cracking events, H-induced ferrite cleavage cracking is the major cracking type, increasing up to 85 % of the total cracks, in the B-doped sample. This means that intergranular cracking along both GBs (γ/γ and α/α) and phase boundaries (α/γ) is less important in causing embrittlement in the B-doped steel, with a minor portion of only 15 % along phase boundaries and other GBs (Fig. 9). This fraction is notably lower than the 60 % intergranular cracking detected in the B-free reference steel (~35 % along phase boundaries, 14 % along ferrite GBs and 11 % along austenite GBs). This observation matches well with the fracture surface characteristics in the H-charged B-doped sample, where only a minor portion of intergranular fracture along multiple interfaces is observed (Fig. 7 (p), ~20 %). We thus conclude that the addition of B and associated interface segregation change the H-induced

fracture mode from a mixed intergranular and cleavage fracture to a transgranular-cleavage-dominated mode. With the foregoing insights, it is possible to imply that B likely suppresses intergranular cracking, which has indeed been extensively documented in previous studies [42–44]. However, the impact of B on ferrite cleavage cracking remains elusive and requires further investigation.

4. Discussion

In contrast to previous studies highlighting the beneficial effect of B on HE resistance in several types of single-phase steels [26,29,42–44], we unexpectedly find that B segregation is rather detrimental to the overall HE resistance of the studied austenite-ferrite two-phase lightweight steel, despite the fact that one specific mechanism, namely, the H-induced intergranular cracking along austenite and ferrite GBs and phase boundaries is notably suppressed. In this section, we discuss this dual role of B on the material's HE behavior, elaborating two major mechanisms: *first*, its effect on mitigating intergranular fracture along these GBs and hetero-interfaces; and *second*, its promoting effect on H diffusion and the resulting enhancement of H abundance and associated local chemical potential, which ultimately deteriorates overall HE resistance. Based on the established insights, we provide guidelines and shed some insights on future H-tolerant alloy design based on segregation engineering.
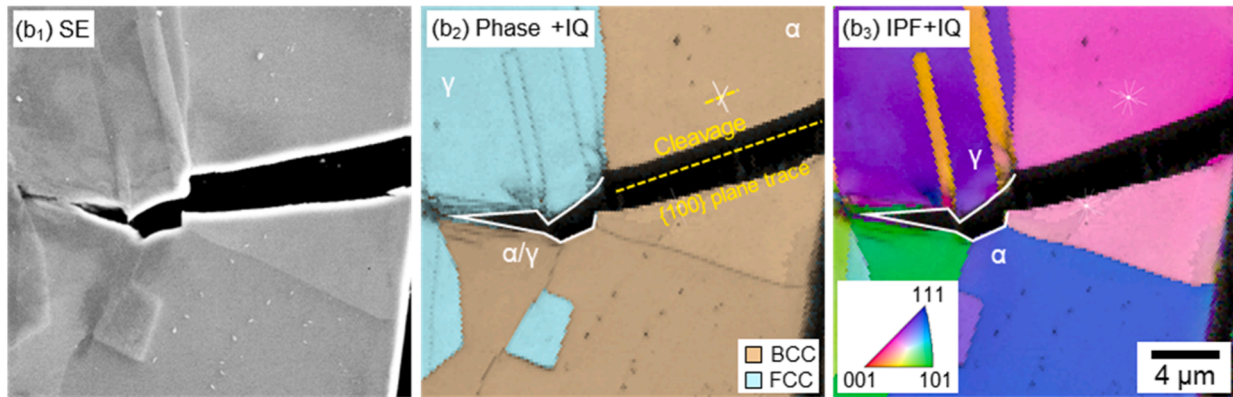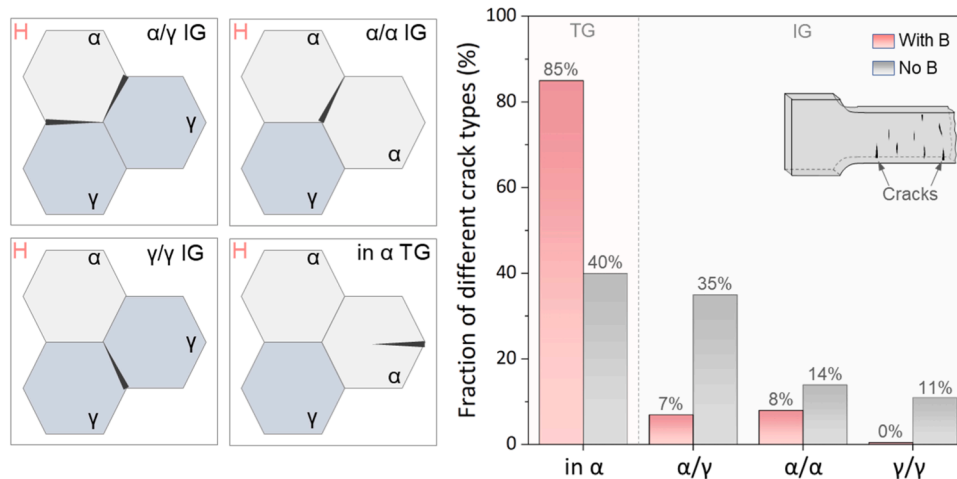
Fig. 8. Correlative secondary electron (SE) imaging and EBSD imaging (including phase plus IQ mapping and IPF) of representative cracks forming along (a) cleavage plane inside ferrite and along ferrite grain boundaries (α/α) and (b) cleavage planes inside ferrite as well as along phase boundaries (α/γ) in the B-doped sample.

Fig. 9. Schematic drawing and quantitative assessments of hydrogen-induced cracks near the specimen surface of the pre-charged and fractured lightweight steels without B and with B. The inset schematically illustrates surface cracks for statistical analysis. The data of the B-free sample were taken from the previous study [9]. (IG: intergranular along grain- and phase boundaries, TG: transgranular cleavage inside ferrite phase).

4.1. The role of interface B segregation in H-induced intergranular cracking

Fracture and damage analyses in Section 3 reveal that the H-induced intergranular cracking along multiple interfaces (γ/γ, α/α and α/γ), is markedly suppressed in the B-doped sample in comparison to the B-free reference material (Figs. 7–9), suggesting enhanced resistance of both of

these interface types to H-induced cracking. H-induced damaging along either the hetero-interfaces or GBs is generally ascribed to the HEDE mechanism [9,41], as the reduction in the cohesive strength of these interfaces is a crucial requirement for advancing crack propagation, otherwise the nucleated cracks would get blunted. Compared to these interfaces in the B-free sample, the key difference in the B-doped sample lies in the significant B segregation at these interfaces, as confirmed in

Figs. 2–4. This B segregation is thus believed to be the core reason for the improved H resistance of these interfaces. The underlying mechanism is here addressed using *ab initio* calculations focusing on two aspects: (1) the effect of B on interface cohesive strength of austenite GBs, ferrite GBs and phase boundaries, and (2) the interplay between B and H.

4.1.1. The effect of B on interface cohesive strength

The role of impurities on interfacial cohesive strength of the aforementioned multiple interfaces, can be generally determined according to the theory of Rice and Wang [46] and Griffith's original work (E_{GW}) on intergranular cracking which can be written as [42,46–49]:

$$E_{GW}^{no\ B/H} = 2\gamma_{free\ surface}^{no\ B/H} - \gamma_{\gamma/\gamma\ GB,\ \alpha/\alpha\ GB,\ \alpha/\gamma\ PB}^{no\ B/H} \tag{5}$$

where $2\gamma_{free\ surface}^{no\ B/H}$ represents the excess free energy per unit area of the newly formed two free surfaces after intergranular fracture, while $\gamma_{\gamma/\gamma\ GB,\ \alpha/\alpha\ GB,\ \alpha/\gamma\ PB}^{no\ B/H}$ refers to the interfacial energy (γ/γ GB, α/α GB and α/γ phase boundary) per unit area. After impurity doping or segregation of B or H, the equation can be modified as:

$$E_{GW}^{B/H\ seg.} = \gamma_{free\ surface}^{no\ B/H} + \gamma_{free\ surface}^{B/H\ seg.} - \gamma_{\gamma/\gamma\ GB,\ \alpha/\alpha\ GB,\ \alpha/\gamma\ PB}^{B/H\ seg.} \tag{6}$$

where $\gamma_{free\ surface}^{B/H\ seg.}$ and $\gamma_{\gamma/\gamma\ GB,\ \alpha/\alpha\ GB,\ \alpha/\gamma\ PB}^{B/H\ seg.}$ indicate the free surface energy per unit area and the GB (γ/γ and α/α) or phase boundary (α/γ) energy per unit area after B/H segregation, respectively. The change of Griffith's work due to B/H segregation can thus be estimated as follows:

$$\Delta E_{GW}^{B/H\ seg.} = \Delta\gamma_{free\ surface}^{B/H\ seg.} - \Delta\gamma_{\gamma/\gamma\ GB,\ \alpha/\alpha\ GB,\ \alpha/\gamma\ PB}^{B/H\ seg.} \tag{7}$$

where $\Delta\gamma_{free\ surface}^{B/H\ seg.} = \gamma_{free\ surface}^{B/H\ seg.} - \gamma_{free\ surface}^{no\ B/H}$, $\Delta\gamma_{\gamma/\gamma\ GB,\ \alpha/\alpha\ GB,\ \alpha/\gamma\ PB}^{B/H\ seg.} = \gamma_{\gamma/\gamma\ GB,\ \alpha/\alpha\ GB,\ \alpha/\gamma\ PB}^{B/H\ seg.} - \gamma_{\gamma/\gamma\ GB,\ \alpha/\alpha\ GB,\ \alpha/\gamma\ PB}^{no\ B/H}$. This theory emphasizes that the role of segregated B/H atoms on brittle intergranular fracture can be assessed by the change in Griffith's work: a positive value of $\Delta E_{GW}^{seg.}$ indicates a suppressed intergranular cracking along both GBs (γ/γ and α/α) and phase boundaries and vice versa.

It has been widely reported in the literature that B segregation can enhance the cohesive strength of different types of interfaces, thus resulting in an increase in Griffith's work [42,47–49]. For example, Kulkov *et al.* [42], using *ab initio* calculations, studied a $\Sigma5(310)$ typed GB in pure Fe. They found that B segregation at this ferrite GB reduced the interfacial energy from 1.38 J/m^2 to -0.51 J/m^2, while also decreasing free surface energy from 4.89 J/m^2 to 4.59 J/m^2. As a result, Griffith's work was increased by 46 % relative to the B-free system, from 3.51 J/m^2 to 5.1 J/m^2, effectively impeding fracture along the ferrite GB. They further attributed this to a chemical effect, where covalent-like bonds between B and the nearest host atoms (Fe) at this boundary lead to GB strengthening. A similar effect of B segregation has also been reported for a $\Sigma5(012)[100]$ symmetrical tilt GB in pure Al, where the formation of Al-B bonds across the GB also leads to an enhancement in fracture resistance [49,50]. Using a first-principle plane-wave pseudopotential method, Hu et al. [51] demonstrated that B increases the hybridization of the bonds in and across a $\Sigma5(210)$ GB in Ni$_3$Al, thereby strengthening its interfacial cohesion. They found that B segregation increases the magnitude of the Griffith work term by 0.22 J/m^2, which results from a reduction of 0.84 J/m^2 in GB energy and of 0.62 J/m^2 in surface energy. These findings support our basic understanding of the main reasons behind the notable strengthening effect of B on various types of austenite and ferrite GBs, here mainly due to the more pronounced reducing effect of B on the GB energy in both phases in comparison to the free surface energy. However, the effect of B segregation on phase boundaries is less understood. In light of these studies about the strengthening influence of B on GBs, we can infer that B segregation is expected to also play a comparable role in increasing the cohesion of phase boundaries. This is to say that B segregation can be assumed to

enhance the magnitude of Griffith's decohesion energy, thereby significantly retarding phase boundary fracture, although this effect has not been reported yet. Such interaction between B atoms and grain/phase boundaries occurs independently of the presence of H, providing an explanation for the suppressed intergranular fracture observed in the investigated steel under H environments.

4.1.2. The effect of B on interface H trapping

It has been well documented in the literature that a critical H concentration is required to trigger decohesion at interfaces [9,41]. As a result, reducing the H content at interfaces might also effectively prevent H-induced intergranular fracture. We first performed *ab initio* calculations to study the possible influence of B segregation on H trapping at a ferrite GB (supplementary note). Given the fact that the consideration of the paramagnetic state, which is the relevant magnetic ordering state for austenite at room temperature within the density functional theory framework is computationally very costly, the direct modelling of the austenite GBs and austenite-ferrite hetero-interface has been omitted in this study. Thus, in this work we focus on a $\Sigma5(210)[001]$ GB in BCC Fe where the magnetic state is ferromagnetic (Fig. 10). The trapping or respectively segregation energies of H at both, B-free and B-doped ferrite GBs were calculated and the results for different trapping sites are listed in Table 3. It is revealed that for most tetrahedral H sites ($T_2 \sim T_3$), the effective segregation energy of H becomes less negative (*i.e.,* decreased segregation tendency) when B is present at the ferrite GB. This result suggests that fewer H atoms will segregate to this interface, as described by the Gibbs adsorption isotherm (Eq. (8)) [52]:

$$\frac{X_H^{\alpha/\alpha\ GB}}{1 - X_H^{\alpha/\alpha\ GB}} = \frac{X_H^{\alpha-bulk}}{1 - X_H^{\alpha-bulk}} \exp\left(-\frac{\Delta E_H^{\alpha/\alpha\ GB}}{k_B T}\right) \tag{8}$$

where $X_H^{\alpha/\alpha\ GB}$ and $X_H^{\alpha-bulk}$ refer to the atomic concentrations of solutes (H) at the ferrite GB and in the BCC Fe bulk, respectively. $\Delta E_H^{\alpha/\alpha\ GB}$ is the segregation energy and k_B represents the Boltzmann constant. It should be noted that B segregation is energetically highly favorable over H segregation, due to its much more negative segregation energy (—0.271 ~ —1.386 eV for B vs. —0.041 ~ —0.222 eV for H). This difference suggests that the available sites within the ferrite GB will be primarily occupied by pre-doped B atoms, which will hence exert a pre-occupation or blocking effect which acts against the subsequent H segregation at the same and even at neighboring sites, due to the B-H repulsion effect.

Although these calculation results have been mainly performed for ferrite GBs due to their tractable ferromagnetic ordering state, we believe that the same principle also applies to other types of interfaces, such as austenite GBs and phase boundaries, an assumption which is
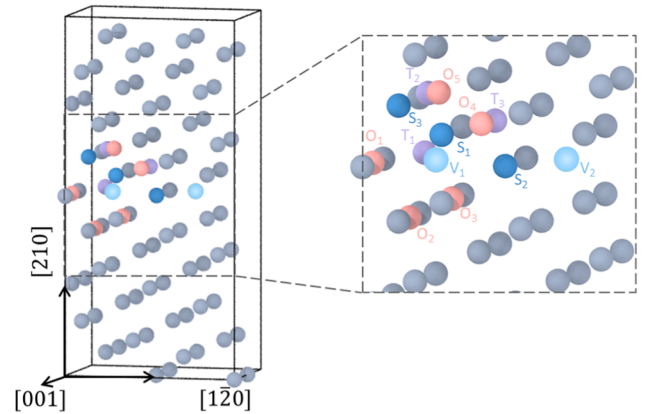
Fig. 10. Schematic illustration of the symmetrical tilt $\Sigma5(210)[100]$ grain boundary in BCC-Fe. The grey spheres denote Fe atoms. Potential segregation or trapping sites are highlighted by spheres of different colors. (O_i: octahedral sites, S_i: substitutional sites, T_i: tetrahedral sites, V_i: voids) [31].

Table 3

Segregation energies of H to various segregation sites as schematically illustrated (T_i: tetrahedral sites) at B-free and B-doped BCC-Fe $\Sigma5(210)$ [001] GB.

Segregation site	Segregation energy of H to BCC-Fe $\Sigma5(210)$[001] GB (eV)		
	B-free GB	B-doped GB (B at voids) [28]	B-doped GB (B at substitutional sites)
T_1	-0.222	0.216	-0.271
T_2	-0.041	0.226	-0.023
T_3	-0.142	0.226	0.78

supported by corresponding literature reports [51,53–55]. For example, a positive interaction energy of 0.17 eV between B and H was documented in FCC Ni$_3$Al [51], unveiling the mutual repulsion between these two elements. Similarly, a repulsive interaction between B and H in FCC CrCoNi alloy has also been described by Ding et al. [53]. They demonstrated that B can occupy the interstitial sites on austenite GBs, and the surrounding sites are energetically much less favorable (prohibited) for further H accumulation, enhancing HE resistance of the austenite GBs. Based on these findings, it is plausible that the site competition between B and H also pertains to phase boundaries in the investigated steels. This is because grain- and phase boundaries are fundamentally similar two-dimensional (2D) interfacial defects, irrespective of the microstructural or compositional differences between the adjacent regions. The consequently reduced H concentration at the interface is another reason accounting for the suppressed intergranular fracture observed in the B-doped sample.

4.2. The role of B segregation on H diffusivity

We next focus on the unexpected and apparently quite detrimental aspects of B addition and segregation. These effects are mainly due to the increase in H diffusion when B is present, hence making larger sample volume portions accessible to H, enlarging the H-affected embrittled zone. Most of the microstructural features such as grain size and phase fraction are unaffected by B and also, the solute content of B in the bulk grain interiors is negligible as discussed above. Therefore, these effects are attributed to the enhanced H diffusivity along the interfaces, leveraging an altogether deeper sample penetration range (Figs. 1–5). The analytical analysis based on the TDS results shows that the effective H diffusion coefficient D_H in the B-doped sample is more than two times higher than in the B-free reference material (8.3×10^{-16} m^2/s vs. 3.0×10^{-16} m^2/s). This doubling of the diffusion coefficient also gives rise to a higher (overall) H concentration/accumulation in the B-doped sample, which is consistent with the experimental observations as shown in Fig. 5 (6.8 ± 2.2 wt ppm vs. 4.7 ± 1.8 wt ppm). As a result, a much larger volume of the B-containing steel becomes accessible to H ingress and uptake, causing embrittlement effects in deep sample regions that would have remained otherwise unaffected by H. This means that although H-induced intergranular cracking is indeed effectively suppressed by B segregation on the interfaces, as elaborated in Section 4.1, the overall much higher H penetration of the steel exceeds this protective effect. Given that the addition of B mainly results in B segregation to interfaces, while other microstructure characteristics remain largely unchanged (Sections 3.1 and 3.2), the enhanced H diffusivity can be firmly attributed to the presence of B at these interfaces, which then doubles the transport coefficient of H along them. More specific, we propose that this counterintuitive effect results from the reduced availability and energy depth of H trapping sites at B-decorated grain- and phase boundaries, and the associated decreased H trapping energy.

Before delving into the underlying mechanisms, it should be noted that the austenite phase of the studied material constitutes a volume fraction of 72 % and percolates throughout the structure. The high phase percolation suggests that H diffusion through the austenite matrix is an inevitable process. However, it must be noted that it is generally reported that H diffusion within the austenite phase is several orders of magnitude slower (2.4×10^{-16} m^2/s at room temperature [56]) compared with that along interfaces (5.8×10^{-12} m^2/s for austenite GBs [57]). This significant difference suggests the negligible role of austenite bulk diffusion, while GB diffusion thus remains as the most likely key factor governing the overall H diffusion range [56–58]. This is supported by several studies on FCC materials including CoCrFeMnNi high-entropy alloys [59,60] and Ni-based alloys [61,62]. In this regard, we learn here that the overall H diffusivity can be highly influenced by interface chemistry, as has also been demonstrated in earlier studies [60, 62,63]. For instance, in a recent study on FCC high-entropy alloy, first-principles calculations suggest that solute Cr enhances H trapping sites at FCC GB due to the attractive interaction between Cr and H, resulting in decreased H diffusivity [60]. Based on *ab initio* calculations, Hickel et al. [63] also demonstrated that strong H trapping at the FCC $\Sigma11$ GB can increase the migration energy required to escape the local minimum, thus raising the diffusion barrier even along GBs.

With respect to the effect of B in the current study, a noticeable enhancement in H diffusion is observed, in contrast to the preceding literature which did not observe this important acceleration effect of B on H diffusion. In contrast, previous research primarily focused on the direct site occupation competition between H and B (or other elements) as well as on repulsive and attractive forces, while overlooking their implications for overall H diffusion along interfaces. This profound accelerating effect observed in this study might stem from a combination of the site competition effect and repulsive interaction between H and B atoms at multiple grain- and phase boundaries. In view of the preceding theoretical analyses and mechanistic discussion, we propose a generalized trapping energy spectrum to elucidate the energetic origin of the facilitated H diffusion and thereby the overall detrimental role of interfacial B segregation on HE resistance (Fig. 11). Based on this energy landscape, it is expected that the majority of the H atoms fall into deeper traps with high trapping energy in the B-free case, as depicted in Fig. 11 (a). Such an H interfacial site occupancy is indicative of lower diffusion kinetics, as the energy penalty of mobilizing an interfacial H atom appears significant. With the occurrence of B segregation, the H trapping behavior at interfaces undergoes certain changes as discussed in Section 4.1. In contrast to the B-free material, B segregation decreases the availability of H trapping sites at both grain- and phase boundaries due to the site competition between B and H atoms [53–55]. As sketched in Fig. 11 (c), pre-doped B atoms occupy the potential H trapping sites. In addition, the *ab initio* calculations (Table 3) show that B reduces the H segregation energy at ferrite GB. Such B-induced reduction effect on H segregation has also been reported for austenite GBs [51,55], thereby lowering its GB decoration according to the Gibbs adsorption isotherm [52]. That is, pre-doped B atoms tend to segregate to the deep trapping sites owing to their high segregation energy compared to H, as reflected in Fig. 11 (d). Consequently, most of the H atoms are constrained to reside in shallower trapping sites associated with lower binding energies. This implies a smaller energy expenditure for (re-)mobilizing an H atom, pushing it back into the diffusive H stream. As a result, the effective overall H migration energy is correspondingly decreased as H is predominantly confined to sites with lower de-trapping energy. In other words, the simulations show that B segregation reduces the availability of deep trapping sites for H by pre-occupying the high-energy traps, and this effect forces H atoms towards occupying weaker trapping sites, thereby also easing de-trapping which lowers the activation energy for H diffusion, leveraging accelerated H diffusion and deeper sample penetration [40]. This effective activation energy reduction constitutes a factor two enhanced H diffusion rate along the interfaces, which ultimately increases the speed of H uptake of the B-doped sample, leading to an enhanced H availability and accumulation and thus exacerbating HE resistance.
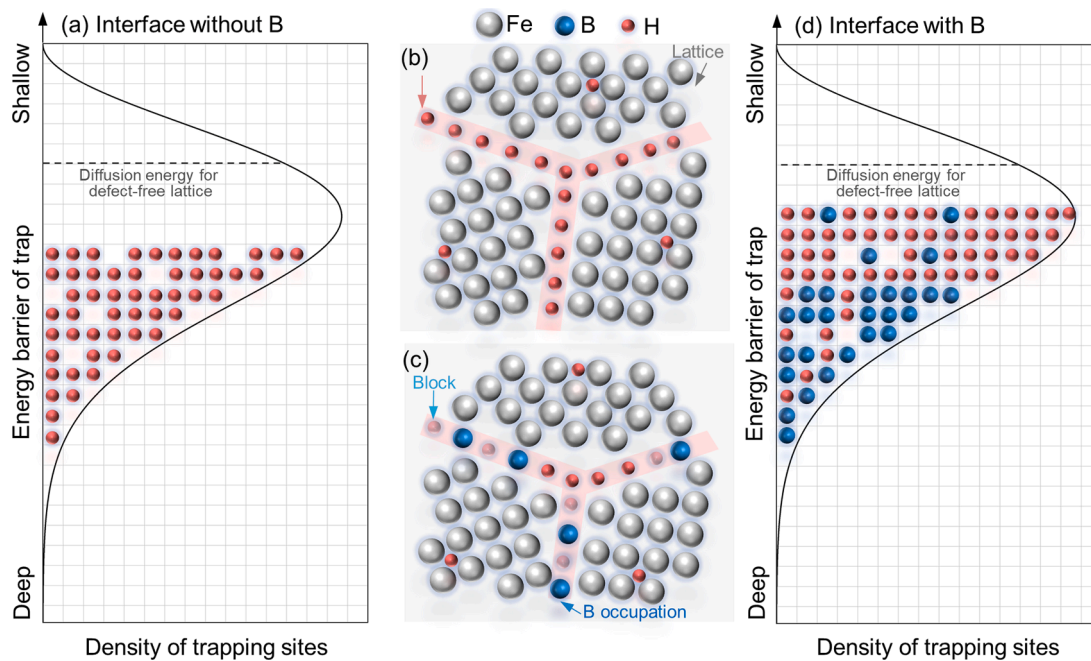
Fig. 11. Schematic plot of energy landscape for interfacial H trapping and the corresponding atomic illustrations in (a)-(b) for the B-free sample and (c)-(d) for the B-doped sample. The dashed lines represent the H diffusion energy barrier which solely depends on the structure of the interface and remains unperturbed by the segregating atoms.

4.3. Implications for H-tolerant microstructure design

The segregation of B has increasingly been established as an effective HE mitigating approach to protect metallic alloys from HE, due to its effect on enhancing the cohesive strength of GBs. This approach has found applications in a range of single-phase metallic alloys (*e.g.,* austenitic steels, martensitic steels, Ni-based alloys, intermetallics and medium/high-entropy alloys [23–29]). The key to its effectiveness lies in the fact that GBs are the most critical junctions and pathways for H transport, trapping and attack, and the resulting intergranular fracture along GBs is the main fracture mechanism under the influence of H. In this case, the strengthening effect of B that protects and strengthens GBs, can pose a beneficial influence on the materials' overall HE resistance, regardless of the enhanced H diffusion kinetics.

However, in stark contrast to previous investigations, B segregation in the investigated steel is also demonstrated to be detrimental to HE resistance. This counterintuitive and quite unexpected result is attributed to the austenite-ferrite microstructure and the associated multiple origins of H-induced damage (austenite and ferrite GBs, phase boundaries and ferrite phase). For this type of lightweight steels where pipe diffusion predominates, H-induced intergranular cracking is not the only damage mode, which renders the B segregation strategy infeasible. The reason is that the suppressed intergranular fracture does not necessarily guarantee the alloy's overall HE resistance, as other HE-related damage modes may become dominant as a result of the accelerated H diffusion and deeper sample penetration, leading to widespread H accumulation and increased H availability over wider sample regions. This is indeed observed in the studied B-doped sample, where H-induced ferrite cleavage cracking along {100} planes is clearly more prevalent over interface cracking (Fig. 9). In this scenario, the effect of B can become rather detrimental on the alloy's overall HE resistance due to the enhanced H diffusivity, as it promotes a more abundant H accumulation altogether throughout the material. Therefore, for the future development of H-tolerant lightweight steels or similar alloys utilizing the B segregation approach, it is crucial to consider not only the H-induced fracture modes but also segregation-associated changes in H transport kinetics and altogether H trapping decrease.

5. Conclusions

We have investigated the role of interface B segregation on HE resistance of two-phase austenite-ferrite lightweight steels (Fe-20Mn-9Al-0.6C-0.009B, wt. %). The effect of B segregation on multiple types of H-induced microstructural damage modes and the B-H interaction and its influence on H diffusivity were revealed and critically discussed. The main conclusions are:

1. Both the B-doped and undoped steels exhibited comparable two-phase microstructures, characterized by nearly identical volume fractions of the constituent austenite and ferrite. B predominantly segregated to both, grain- and phase boundaries. Its content in bulk grains was negligible. Interfacial segregation in the B-free sample was also negligible. In the absence of H, the mechanical properties were unaffected by B. However, surprisingly, the addition of B exacerbated the alloy's overall HE resistance compared to the B-free reference steel, with a ductility loss increasing from ~28 % (B-free) to ~44 % (B-doped) in the presence of H.
2. Post-mortem fractographic and H-induced cracking analyses revealed that B doping and its pronounced interface segregation at ferrite GBs, austenite GBs and ferrite-austenite phase boundaries, shifted the H-induced fracture mode from a mixed intergranular damage mode along these interfaces (~60 %) and cleavage fracture inside ferrite phase (~40 %) to a cleavage-dominated mode (~80 %). This transition unravelled a dual-role nature of B segregation in H-induced damage: it mitigated intergranular fracture while cleavage fracture within ferrite became dominant.
3. The effectiveness of B segregation in impeding H-related intergranular fracture was primarily attributed to its enhancing effect on interfacial cohesive strength of grain- and phase boundaries, and the suppressed H trapping at these interfaces caused by the repulsive interplay with B, as evidenced by the *ab initio* calculations of the effects of B at a ferrite GB.
4. The H-induced cleavage cracking within ferrite phase accounted for ~85 % of all probed cracking events (~40 % in the B-free reference sample). This promoted cleavage fracture was associated with the

accelerated diffusivity of H and the resulting increase in H abundance and widespread accessibility as suggested by TDS and fractography analyses. Such acceleration was explained by the reduced available trapping sites and decreased H migration energy barrier due to the site competition effect as well as repulsive interaction between B and H.

5. To advance the design of H-tolerant lightweight steels and related alloys, leveraging the B segregation strategy, it is thus essential to account not only for H-induced fracture modes and secure B-related GB cohesive strengthening but also consider microstructure- and chemistry-related measures to control or even suppress the B-associated enhancement in weaker H trapping and enhanced overall H migration kinetics.

CRediT authorship contribution statement

Xizhen Dong: Writing – review & editing, Writing – original draft, Visualization, Validation, Methodology, Investigation, Formal analysis, Data curation, Conceptualization. **Shaolou Wei:** Writing – review & editing. **Ali Tehranchi:** Writing – review & editing, Software. **Aparna Saksena:** Writing – review & editing. **Dirk Ponge:** Writing – review & editing, Supervision. **Binhan Sun:** Writing – review & editing, Supervision. **Dierk Raabe:** Writing – review & editing, Supervision, Project administration.

Declaration of competing interest

The authors declare that they have no known competing financial interests or personal relationships that could have appeared to influence the work reported in this paper.

Acknowledgements

Supplementary materials

Supplementary material associated with this article can be found, in the online version, at doi:10.1016/j.actamat.2025.121458.

References

[1] D. Raabe, B. Sun, A. Kwiatkowski Da Silva, B. Gault, H.-W. Yen, K. Sedighiani, P. Thoudden Sukumar, I.R. Souza Filho, S. Katnagallu, E. Jägle, Current challenges and opportunities in microstructure-related properties of advanced high-strength steels, Metall. Mater. Trans. A 51 (2020) 5517–5586.

[2] J. Hu, X. Li, Q. Meng, L. Wang, Y. Li, W. Xu, Tailoring retained austenite and mechanical property improvement in Al–Si–V containing medium Mn steel via direct intercritical rolling, Mater. Sci. Eng. A 855 (2022) 143904.

[3] D. Raabe, H. Springer, I. Gutiérrez-Urrutia, F. Roters, M. Bausch, J.-B. Seol, M. Koyama, P.-P. Choi, K. Tsuzaki, Alloy design, combinatorial synthesis, and microstructure–property relations for low-density Fe-Mn-Al-C austenitic steels, Jom 66 (2014) 1845–1856.

[4] S.S. Sohn, K. Choi, J.-H. Kwak, N.J. Kim, S. Lee, Novel ferrite–austenite duplex lightweight steel with 77% ductility by transformation induced plasticity and twinning induced plasticity mechanisms, Acta Mater. 78 (2014) 181–189.

[5] A. Zargaran, H. Kim, J. Kwak, N.J. Kim, Effects of Nb and C additions on the microstructure and tensile properties of lightweight ferritic Fe–8Al–5Mn alloy, Scr Mater. 89 (2014) 37–40.

[6] J. Moon, S.-J. Park, J.H. Jang, T.-H. Lee, C.-H. Lee, H.-U. Hong, H.N. Han, J. Lee, B. H. Lee, C. Lee, Investigations of the microstructure evolution and tensile deformation behavior of austenitic Fe-Mn-Al-C lightweight steels and the effect of Mo addition, Acta Mater. 147 (2018) 226–235.

[7] M. Koyama, H. Springer, S.V. Merzlikin, K. Tsuzaki, E. Akiyama, D. Raabe, Hydrogen embrittlement associated with strain localization in a precipitation-hardened Fe–Mn–Al–C light weight austenitic steel, Int. J. Hydrog. Energy 39 (2014) 4634–4646.

[8] S.W. Hwang, J.H. Ji, E.G. Lee, K.-T. Park, Tensile deformation of a duplex Fe–20Mn–9Al–0.6 C steel having the reduced specific weight, Mater. Sci. Eng. A 528 (2011) 5196–5203.

[9] X. Dong, D. Wang, P. Thoudden-Sukumar, A. Tehranchi, D. Ponge, B. Sun, D. Raabe, Hydrogen-associated decohesion and localized plasticity in a high-Mn and high-Al two-phase lightweight steel, Acta Mater. 239 (2022) 118296.

[10] M.C. Ha, J.-M. Koo, J.-K. Lee, S.W. Hwang, K.-T. Park, Tensile deformation of a low density Fe–27Mn–12Al–0.8 C duplex steel in association with ordered phases at ambient temperature, Mater. Sci. Eng. A 586 (2013) 276–283.

[11] J. Hu, X. Li, Z. Zhang, L. Wang, Y. Li, W. Xu, Overcoming the strength-ductility trade-off in metastable dual-phase heterogeneous structures using variable temperature rolling and annealing, Mater. Res. Lett. 11 (2023) 648–654.

[12] J. Yoo, M.C. Jo, D.W. Kim, H. Song, M. Koo, S.S. Sohn, S. Lee, Effects of Cu addition on resistance to hydrogen embrittlement in 1 GPa-grade duplex lightweight steels, Acta Mater. 196 (2020) 370–383.

[13] J. Moon, H.-H. Jo, S.-J. Park, S.-D. Kim, T.-H. Lee, C.-H. Lee, M.-G. Lee, H.-U. Hong, D.-W. Suh, D. Raabe, Ti-bearing lightweight steel with large high temperature ductility via thermally stable multi-phase microstructure, Mater. Sci. Eng. A 808 (2021) 140954.

[14] B. Sun, W. Lu, B. Gault, R. Ding, S.K. Makineni, D. Wan, C.-H. Wu, H. Chen, D. Ponge, D. Raabe, Chemical heterogeneity enhances hydrogen resistance in high-strength steels, Nat. Mater. 20 (2021) 1629–1634.

[15] M. Okayasu, M. Sato, D. Ishida, T. Senuma, The effect of precipitations (NbC and carbide) in Fe–C–Mn-xNb steels on hydrogen embrittlement characteristics, Mater. Sci. Eng. A 791 (2020) 139598.

[16] J. Lee, T. Lee, D.-J. Mun, C.M. Bae, C.S. Lee, Comparative study on the effects of Cr, V, and Mo carbides for hydrogen-embrittlement resistance of tempered martensitic steel, Sci. Rep. 9 (2019) 5219.

[17] H. Khalid, V.C. Shunmugasamy, R.W. DeMott, K. Hattar, B. Mansoor, Effect of grain size and precipitates on hydrogen embrittlement susceptibility of nickel alloy 718, Int. J. Hydrog. Energy 55 (2024) 474–490.

[18] A. Oudriss, J. Creus, J. Bouhattate, E. Conforto, C. Berziou, C. Savall, X. Feaugas, Grain size and grain-boundary effects on diffusion and trapping of hydrogen in pure nickel, Acta Mater. 60 (2012) 6814–6828.

[19] M. Koyama, K. Ichii, K. Tsuzaki, Grain refinement effect on hydrogen embrittlement resistance of an equiatomic CoCrFeMnNi high-entropy alloy, Int. J. Hydrog. Energy 44 (2019) 17163–17167.

[20] S. Bechtle, M. Kumar, B.P. Somerday, M.E. Launey, R.O. Ritchie, Grain-boundary engineering markedly reduces susceptibility to intergranular hydrogen embrittlement in metallic materials, Acta Mater. 57 (2009) 4148–4157.

[21] M. Seita, J.P. Hanson, S. Gradečak, M.J. Demkowicz, The dual role of coherent twin boundaries in hydrogen embrittlement, Nat. Commun. 6 (2015) 6164.

[22] Q. Sun, Q. Han, J. Li, F. Cao, S. Wang, Tailoring hydrogen embrittlement resistance of pure Ni by grain boundary engineering, Corros. Commun. 6 (2022) 48–51.

[23] K. Okada, A. Shibata, T. Sasaki, H. Matsumiya, K. Hono, N. Tsuji, Improvement of resistance against hydrogen embrittlement by controlling carbon segregation at prior austenite grain boundary in 3Mn-0.2 C martensitic steels, Scr Mater. 224 (2023) 115043.

[24] J. Yoo, M.C. Jo, M.C. Jo, S. Kim, S.-H. Kim, J. Oh, S.S. Sohn, S. Lee, Effects of solid solution and grain-boundary segregation of Mo on hydrogen embrittlement in 32MnB5 hot-stamping steels, Acta Mater. 207 (2021) 116661.

[25] B. Zhang, K. Xiong, M. Wang, Z. Liu, K. Shen, Y. Mao, H. Chen, Grain boundary alloying segregation to resist hydrogen embrittlement in BCC-Fe steels: atomistic insights into solute-hydrogen interactions, Scr Mater. 238 (2024) 115757.

[26] C. Liu, E. George, W. Oliver, Grain-boundary fracture and boron effect in Ni3Si alloys, Intermetallics 4 (1996) 77–83.

[27] E. George, C. Liu, H. Lin, D. Pope, Environmental embrittlement and other causes of brittle grain boundary fracture in Ni3Al, Mater. Sci. Eng. A 192 (1995) 277–288.

[28] G. Hachet, A. Tehranchi, H. Shi, M. Prabhakar, S. Wei, K. Angenendt, S. Zaefferer, B. Gault, B. Sun, D. Ponge, Segregation at prior austenite grain boundaries: the competition between boron and hydrogen, Int. J. Hydrog. Energy 95 (2024) 734–746.

[29] X. Chen, X. Zhuang, J. Mo, J. He, T. Yang, X. Zhou, W. Liu, Enhanced resistance to hydrogen embrittlement in a CrCoNi-based medium-entropy alloy via grain-boundary decoration of boron, Mater. Res. Lett. 10 (2022) 278–286.

[30] M. Herbig, P. Choi, D. Raabe, Combining structural and chemical information at the nanometer scale by correlative transmission electron microscopy and atom probe tomography, Ultramicroscopy 153 (2015) 32–39.

[31] X. Dong, A. Saksena, A. Tehranchi, B. Gault, D. Ponge, B. Sun, D. Raabe, Interfacial boron segregation in a high-Mn and high-Al multiphase lightweight steel, Acta Mater. 283 (2025) 120568.

[32] B.H. Toby, R.B. Von Dreele, GSAS-II: the genesis of a modern open-source all purpose crystallography software package, Appl. Crystallogr. 46 (2013) 544–549.

[33] S. Wei, C.C. Tasan, Deformation faulting in a metastable CoCrNiW complex concentrated alloy: a case of negative intrinsic stacking fault energy? Acta Mater. 200 (2020) 992–1007.

[34] L. Claeys, V. Cnockaert, T. Depover, I. De Graeve, K. Verbeken, Critical assessment of the evaluation of thermal desorption spectroscopy data for duplex stainless

steels: a combined experimental and numerical approach, Acta Mater. 186 (2020) 190–198.

[35] A. Hussein, M. Cauwels, L. Claeys, T. Depover, K. Verbeken, A full-field model for hydrogen diffusion and trapping in two-phase microstructures: application to thermal desorption spectroscopy of duplex stainless steel, Acta Mater. (2025) 121042.

[36] L. Claeys, T. Depover, I. De Graeve, K. Verbeken, Electrochemical hydrogen charging of duplex stainless steel, Corrosion 75 (2019) 880–887.

[37] J. Crank, The mathematics of diffusion, Oxford university press, 1979.

[38] C.San Marchi, B.P. Somerday, S.L. Robinson, Permeability, solubility and diffusivity of hydrogen isotopes in stainless steels at high gas pressures, Int. J. Hydrog. Energy 32 (2007) 100–116.

[39] E. Owczarek, T. Zakroczymski, Hydrogen transport in a duplex stainless steel, Acta Mater. 48 (2000) 3059–3070.

[40] A. Turk, S.D. Pu, D. Bombač, P.E. Rivera-Díaz-del-Castillo, E.I. Galindo-Nava, Quantification of hydrogen trapping in multiphase steels: part II–Effect of austenite morphology, Acta Mater. 197 (2020) 253–268.

[41] B. Sun, W. Krieger, M. Rohwerder, D. Ponge, D. Raabe, Dependence of hydrogen embrittlement mechanisms on microstructure-driven hydrogen distribution in medium Mn steels, Acta Mater. 183 (2020) 313–328.

[42] S.S. Kulkov, A.V. Bakulin, S.E. Kulkova, Effect of boron on the hydrogen-induced grain boundary embrittlement in α-Fe, Int. J. Hydrog. Energy 43 (2018) 1909–1925.

[43] H. Li, X. Cheng, H. Shen, L. Su, S. Zhang, Effect of boron microalloying element on susceptibility to hydrogen embrittlement in high strength mooring chain steel, HSLA Steels, in: Microalloying 2015 & Offshore Engineering Steels 2015: Conference Proceedings, Wiley Online Library, 2015, 2015, pp. 1211–1218.

[44] A.S. Kholtobina, W. Ecker, R. Pippan, V.I. Razumovskiy, Effect of alloying elements on hydrogen enhanced decohesion in bcc iron, Comput. Mater. Sci. 188 (2021) 110215.

[45] A.A. Guzmán, J. Jeon, A. Hartmaier, R. Janisch, Hydrogen embrittlement at cleavage planes and grain boundaries in bcc iron—Revisiting the first-principles cohesive zone model, Mater 13 (2020) 5785.

[46] J.R. Rice, J.-S. Wang, Embrittlement of interfaces by solute segregation, Mater. Sci. Eng. A 107 (1989) 23–40.

[47] R. Janisch, C. Elsässer, Segregated light elements at grain boundaries in niobium and molybdenum, Phys. Rev. B 67 (2003) 224101.

[48] S. Kulkova, A. Bakulin, S. Kulkov, S. Hocker, S. Schmauder, Hydrogen sorption in titanium alloys with a symmetric Σ5 (310) tilt grain boundary and a (310) surface, J. Exp. Theor. Phys. 115 (2012) 462–473.

[49] R. Wu, A. Freeman, G.B. Olson, First principles determination of the effects of phosphorus and boron on iron grain boundary cohesion, Science 265 (1994) 376–380.

[50] S. Zhang, O.Y. Kontsevoi, A.J. Freeman, G.B. Olson, First-principles determination of the effect of boron on aluminum grain boundary cohesion, Phys. Rev. B 14Condensed Matter. Mater. Phys. 84 (2011) 134104.

[51] Q. Hu, R. Yang, D. Xu, Y. Hao, D. Li, W. Wu, Energetics and electronic structure of grain boundaries and surfaces of B-and H-doped Ni 3 Al, Phys. Rev. B 67 (2003) 224203.

[52] P. Lejcek, Grain boundary segregation in metals, Springer Science & Business Media, 2010.

[53] C. Ding, Z. Jiao, J. Luan, B. Xu, R. Li, B. Cao, C. Zhou, W. Liu, Suppressing hydrogen embrittlement of a CrCoNi medium-entropy alloy by triggering co-segregation of carbon, boron, and Cr, Corros. Sci. 236 (2024) 112232.

[54] S.E. Kulkova, A. Bakulin, S. Kulkov, S. Hocker, S. Schmauder, Influence of interstitial impurities on the Griffith work in Ti-based alloys, Phys. Scr 90 (2015) 094010.

[55] F.-H. Wang, J.-X. Shang, J.-M. Li, C.-Y. Wang, The effects of boron and hydrogen on the embrittlement of polycrystalline Ni3Al, Intermetallics 8 (2000) 589–593.

[56] Y. Mine, K. Tachibana, Z. Horita, Effect of high-pressure torsion processing and annealing on hydrogen embrittlement of type 304 metastable austenitic stainless steel, Metall. Mater. Trans. A 41 (2010) 3110–3120.

[57] J. Lee, C. Park, H. Park, N. Kang, Effective hydrogen diffusion coefficient for CoCrFeMnNi high-entropy alloy and microstructural behaviors after hydrogen permeation, Int. J. Hydrog. Energy 45 (2020) 10227–10232.

[58] S. Chan, S. Lee, H. Yang, Effect of retained austenite on the hydrogen content and effective diffusivity of martensitic structure, Metall. Trans. A 22 (1991) 2579–2586.

[59] O. Kazum, H. Beladi, M.B. Kannan, Hydrogen permeation in twinning-induced plasticity (TWIP) steel, Int. J. Hydrog. Energy 43 (2018) 22685–22693.

[60] S.C. Marques, A.V. Castilho, D.S. dos Santos, Effect of alloying elements on the hydrogen diffusion and trapping in high entropy alloys, Scr Mater. 201 (2021) 113957.

[61] A. Turnbull, R. Ballinger, I. Hwang, M. Morra, M. Psaila-Dombrowski, R. Gates, Hydrogen transport in nickel-base alloys, Metall. Trans. A 23 (1992) 3231–3244.

[62] C. Hurley, F. Martin, L. Marchetti, J. Chêne, C. Blanc, E. Andrieu, Role of grain boundaries in the diffusion of hydrogen in nickel base alloy 600: study coupling thermal desorption mass spectroscopy with numerical simulation, Int. J. Hydrog. Energy 41 (2016) 17145–17153.

[63] T. Hickel, R. Nazarov, E. McEniry, G. Leyson, B. Grabowski, J. Neugebauer, Ab initio based understanding of the segregation and diffusion mechanisms of hydrogen in steels, JOM 66 (2014) 1399–1405.